The role of crystal packing on the optical response of trialkyltetrelethynyl acenes

Cite as: J. Chem. Phys. 157, 084703 (2022); doi: 10.1063/5.0097421

Submitted: 28 April 2022 • Accepted: 15 July 2022 •

Published Online: 23 August 2022











Ling-Yi Huang, D Qianxiang Ai, D and Chad Risko D



AFFILIATIONS

Department of Chemistry and Center for Applied Energy Research, University of Kentucky, Lexington, Kentucky 40506, USA

Note: This paper is part of the JCP Special Topic on Photophysics in Emerging Photovoltaics.

a) Author to whom correspondence should be addressed: chad.risko@uky.edu

ABSTRACT

The electronic and optical responses of an organic semiconductor (OSC) are dictated by the chemistries of the molecular or polymer building blocks and how these chromophores pack in the solid state. Understanding the physicochemical nature of these responses is not only critical for determining the OSC performance for a particular application, but the UV/visible optical response may also be of potential use to determine aspects of the molecular-scale solid-state packing for crystal polymorphs or thin-film morphologies that are difficult to determine otherwise. To probe these relationships, we report the quantum-chemical investigation of a series of trialkyltetrelethynyl acenes (tetrel = silicon or germanium) that adopt the brickwork, slip-stack, or herringbone (HB) packing configurations; the π -conjugated backbones considered here are pentacene and anthradithiophene. For comparison, HB-packed (unsubstituted) pentacene is also included. Density functional theory and G₀W₀ (single-shot Green's function G and/or screened Coulomb function W) electronic band structures, G₀W₀-Bethe-Salpeter equation-derived optical spectra, polarized ϵ_2 spectra, and distributions of both singlet and triplet exciton wave functions are reported. Configurational disorder is also considered. Furthermore, we evaluate the probability of singlet fission in these materials through energy conservation relationships.

Published under an exclusive license by AIP Publishing. https://doi.org/10.1063/5.0097421

INTRODUCTION

Organic semiconductors (OSCs) have attracted considerable attention because of their promise in low-power, lightweight, flexible, and high-performance electronic and optoelectronic devices, such as field-effect transistors, 1-9 light-emitting diodes, 10-16 and photovoltaics. 17-24 From a fundamental perspective, OSCs offer distinct opportunities to explore physical phenomena that differ from those exhibited by conventional inorganic semiconductors, as OSC building blocks are held together by weak noncovalent interactions when compared to the strong covalent bonds, ionic bonds, and permutations thereof among the atomic building blocks of inorganic materials. These non-covalent interactions in OSC, notably, allow for varied means of manufacture through vapor or solution processes.^{25,26} For instance, vapor processing [e.g., physical vapor transport (PVT)] can be used to produce high-quality organic crystals, while solution processing techniques are more suitable for the production of large-area [(semi-)crystalline, amorphous, and combinations thereof] thin films.

The solid-state arrangements of the π -conjugated molecular or polymer building blocks of an OSC ultimately determine the material's electronic and optical responses. Here, we focus on OSC molecular crystals for which several distinct molecular packing motifs have been identified. In particular, three arrangements (Fig. 1) are often reported for molecules that have sizable longaxis-to-short-axis aspect ratios (e.g., pentacene): Herringbone (HB), brickwork (BW), and slip stack (SS).^{27,28} In classic HB packing, a molecule and its neighbors are arranged in an edge-to-face orientation; HB packing is often found for molecules that have no or small chemical substituents attached to the π -conjugated core. BW and SS motifs, on the other hand, are realized through chemical substitution with bulky substituents. In the BW motif [Fig. 1(a)], the molecules present a two-dimensional (2D), face-to-face stacking arrangement of the π -conjugated backbone of a molecule and the backbones of four of its neighbors. The SS motif [Fig. 1(b)], on the other hand, presents a one-dimensional (1D), face-to-face stacking arrangement of the π -conjugated backbone of a molecule with only two of its neighbors. All three packing arrangements can lead to large intermolecular electronic couplings (transfer integrals) that

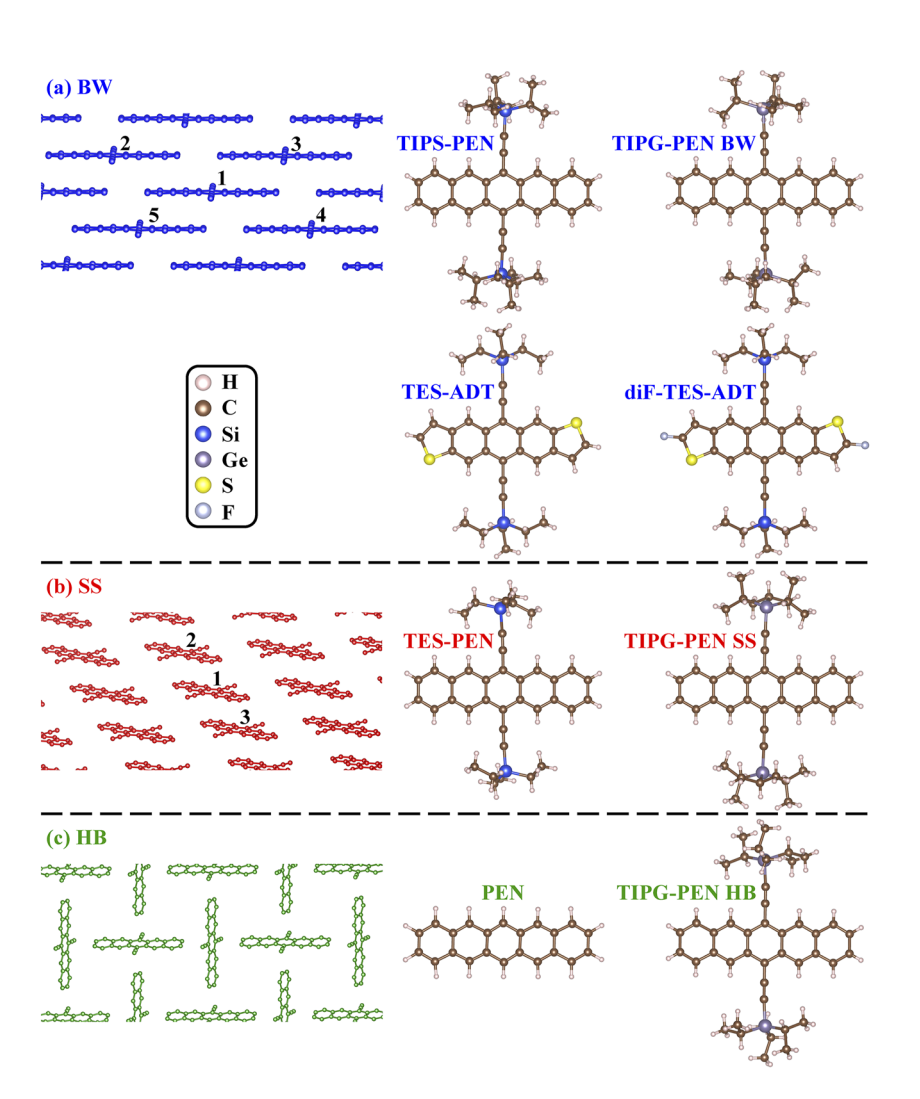


FIG. 1. Three common OSC packing motifs. Molecular packings in the brickwork (BW), slip-stack (SS), and herringbone (HB) motifs are shown in the left column of (a), (b), and (c), respectively. For clarity, only the backbones are displayed. Color is used to represent the different packing motifs: BW in blue, SS in red, and HB in green. The second and third columns show the molecular structures studied in this work.

influence the crystal's electronic and optical properties. Note that organic molecules often form crystals with different packing motifs in ambient conditions, i.e., polymorphs.^{29–31}

Here, we are interested in delineating how the HB, BW, and SS packing arrangements impact the electronic and optical properties of trialkyltetrelethynyl acenes (tetrel = silicon or germanium), where the acene is either pentacene (PEN) or anthradithophene (ADT). The materials studied include (unsubstituted) pentacene, 6,13-bis(triisopropylsilylethynyl) pentacene (TIPS-PEN), 6,13-bis(triisopropylgermanylethynyl) pentacene (TIPG-PEN), 6,13-bis(triethylsilylethynyl) pentacene (TES-PEN), 5,11-bis(triethylsilylethynyl) anthradithiophene (TES-ADT), and 2,8-difluoro-5,11-bis(triethylsilylethynyl) anthradithiophene (diF-TES-ADT). In particular, we investigate the following: (i) how the varied molecular chemistries and packing motifs impact the electronic and optical properties, (ii) the possibilities to distinguish the molecular packing of OSC crystals through their optical response, and (iii) the propensity for these materials to undergo singlet fission.

COMPUTATIONAL METHODS

Experimental crystal structures determined by single-crystal x-ray diffraction were employed in this study, with no further unit cell or molecular geometry relaxation. This choice was made, in part, as we are interested in deriving ways to identify optical properties of experimentally relevant packing motifs through computational approaches. The crystal structures can be obtained/downloaded from the Cambridge Crystallographic Data Center (CCDC).³² Additional meta-data, both experimental and computational, pertaining to these systems can be accessed in the Organic Crystals in Electronic and Light-Oriented Technologies (OCELOT) database.³³ CCDC deposition numbers and OCELOT identification (ID) numbers are listed in Table I. Note that the crystal structures downloaded from CCDC may contain disorder, while those from OCELOT have had disorder removed. The types of disorder found in these molecular crystals will be discussed in the section titled Results and

Initial density functional theory (DFT) calculations were performed using the Quantum ESPRESSO plane-wave code^{34,35} with

TABLE I. CCDC (Cambridge Crystallographic Data Center) deposition numbers and OCELOT (Organic Crystals in Electronic and Light-Oriented Technologies) identification (ID) numbers of materials considered in this work with the identified packing configurations.

Material	CCDC number	OCELOT number	Packing
TIPS-PEN	172 476	com_k01029	BW
TIPG-PEN BW	1 889 786	com_x17059	BW
TES-ADT	269 924	com_k04014	BW
diF-TES-ADT	1 406 651	com_x14203	BW
TES-PEN	1 028 702	com_k01066	SS
TIPG-PEN SS	1 889 787	com_x17061	SS
PEN	1 230 799	csd_PENCEN	HB
TIPG-PEN HB	1 889 788	com_k13114s	HB

pseudopotentials generated by the ONCVPSP (Optimized Norm-Conserving Vanderbilt Pseudopotential) code³⁶ coupled with the Perdew, Burke, and Ernzerhof (PBE) exchange–correlation functional.³⁷ We include 1 (1s¹), 4 (2s²2p²), 7 (2s²2p⁵), 4 (3s²3p²), 6 (3s²3p⁴), and 14 (3d¹04s²4p²) electrons as valence electrons for H, C, F, Si, S, and Ge, respectively, and their core cutoff radii are 0.70, 1.20, 0.95, 1.60, 1.40, and 1.75 a.u., respectively. An energy cutoff of 1088 eV was used with k-point meshes of $4 \times 2 \times 5$, $4 \times 2 \times 4$, $4 \times 4 \times 2$, $4 \times 3 \times 3$, $2 \times 2 \times 2$, $4 \times 3 \times 3$, $4 \times 4 \times 2$, and $4 \times 4 \times 2$ for PEN, TIPS-PEN, TIPG-PEN BW, TIPG-PEN SS, TIPG-PEN HB, TES-PEN, TES-ADT, and diF-TES-ADT, respectively.

The results of the DFT calculations were used as input for the BerkeleyGW package $^{38-40}$ to carry out G_0W_0 -Bethe-Salpeter

equation (BSE) calculations. As we aim to investigate the electronic and optical properties of molecular crystals with 72–100 ions/atoms per unit cell, self-consistent GW (the Green's function G and/or screened Coulomb function W are updated self-consistently) is an approach that is generally too computationally expensive. Furthermore, it has been shown for organic crystals that self-consistent GW can produce results that are in poor agreement with experiment when compared to single-shot GW, denoted G_0W_0 , with a generalized gradient approximation (GGA) starting point. Hence, we made use of G_0W_0 in this study. 792 bands were included to determine the dielectric function and self-energy for all materials, with 163 eV for the dielectric function planewave cutoff. The BSE is solved under the Tamm–Dancoff 43,44 and static approximations. Band structures were plotted by the Wannier90 code. 45

RESULTS AND DISCUSSION

Impact of molecular disorder

Two types of molecular disorder are considered to understand their influence on the crystal's electronic and optical properties. First, disorder manifest in the side chains (as shown in the top panel of Fig. 2) occurs when the side-chain orientations differ, e.g., as exhibited by the top right (and, by symmetry, the bottom left) C_3H_7 that is connected to Si (or Ge). TIPS-PEN and TIPG-PEN in the BW packing present this type of disorder. The most probable configuration has the lowest total energy (labeled L), while the least probable configuration has the highest total energy (labeled H). The second disorder type considers the location of heteroatoms

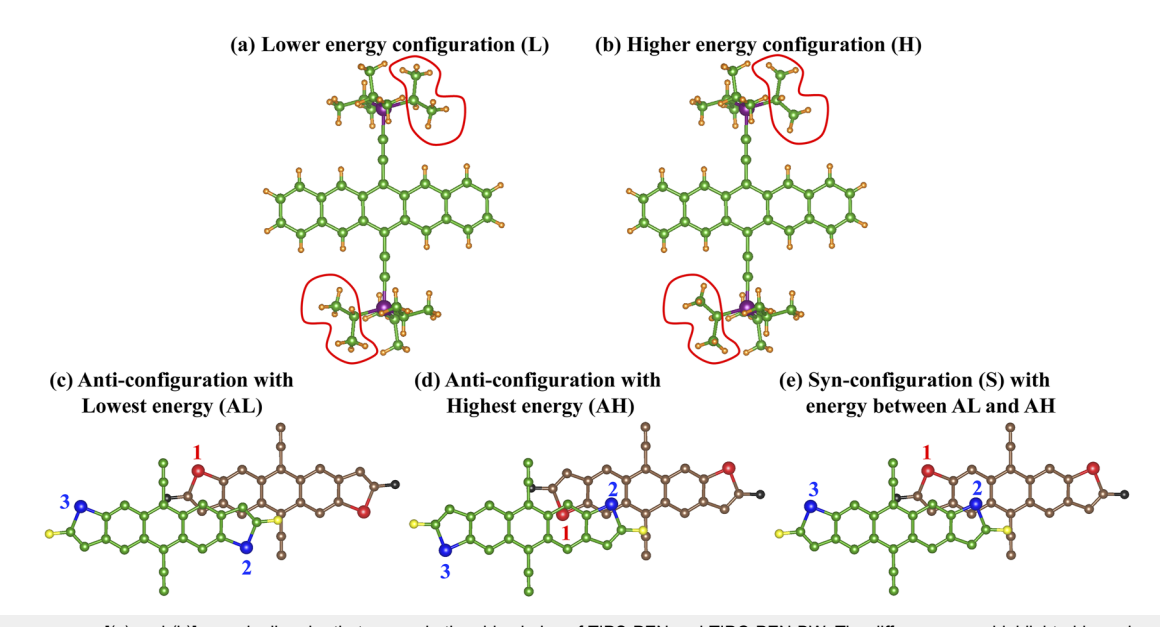
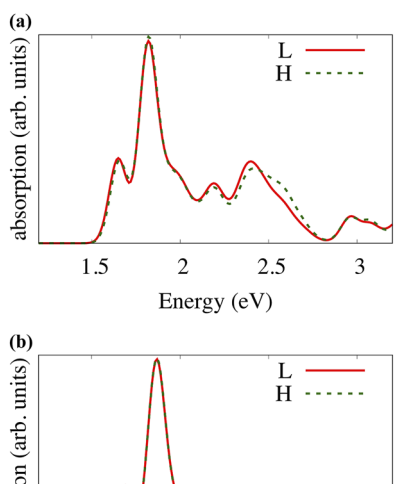


FIG. 2. The upper row [(a) and (b)] reveals disorder that occurs in the side chains of TIPS-PEN and TIPG-PEN BW. The differences are highlighted by red surfaces. The lower row [(c)–(e)] shows the disorder that can occur in the anthradithiophene (ADT) backbones of TES-ADT and diF-TES-ADT; for clarity, the side chains and H atoms are not displayed, and the adjacent backbones are displayed in different colors. C atoms are represented by green and brown spheres, hydrogen atoms are represented by orange spheres, Si (or Ge) atoms are represented by purple spheres, sulfur atoms are represented by blue and red spheres, and F atoms are represented by yellow and black spheres, respectively.

in the π -conjugated backbone—here, occurring for systems with the anthradithiophene (ADT) backbone. 46-50 When accounting for this kind of disorder, there are several potential variations in the packing based on the sulfur positions (anti- vs syn-) in the carbon framework.⁵⁰ Here, we consider three packing motifs that depend on anti- or syn-positioning of the sulfur atoms, as depicted in the bottom panel of Fig. 2: (i) for the anti-configuration of the sulfur atoms in the backbone, the sulfur atoms in the neighboring molecules are placed at the farthest inter-sulfur distance possible, a configuration that leads to the lowest total energy (labeled AL); (ii) for the anti-configuration of the sulfur atoms in the backbone, the sulfur atoms in the neighboring molecules are made to be in close contact, a configuration resulting in the highest total energy of the three configurations considered (labeled AH); and, (iii) for the syn-configuration of the sulfur atoms in the backbone, the molecules are arranged where the sulfur atoms in all molecules are oriented in the same direction, a configuration resulting in a total energy that lies between the two anti-configurations (labeled S).

The electronic band structures of TIPS-PEN and TIPG-PEN BW, each with disordered side chains, determined at the G_0W_0 level are shown in Fig. 3, and the calculated absorption spectra determined at the G_0W_0 -BSE level are shown in Fig. 4. From the upper panel of Fig. 3, one observes that the band structures of the L and H configurations of TIPS-PEN are similar, with exceptions arising in the high energy bands [i.e., those 3 eV higher than the conduction band (CB)]. For TIPG-PEN BW, the band structures of the L and H configurations are identical (lower panel of Fig. 3). For both TIPS-PEN and TIPG-PEN BW, the electronic bandgaps and bandwidths of the valence band (VB) and conduction band (CB) are the same for both the L and H configurations. Figure 4 shows absorption spectra of TIPS-PEN and TIPG-PEN BW



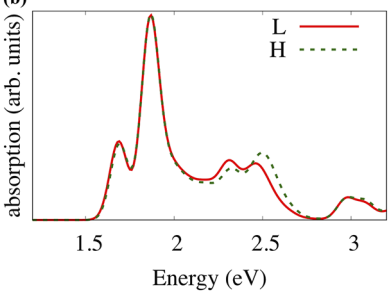


FIG. 4. Absorption spectra of (a) TIPS-PEN and (b) TIPG-PEN BW using the G_0W_0 -BSE approach. L (H) stands for the lower (higher) energy configuration as defined in the upper panel of Fig. 2. The intensities of first peaks are normalized.

in the L (solid red curves) and H (dotted green curves) configurations. In both cases, the spectra for the lower energy configurations are almost coincident with that of the higher energy configurations, with exceptions occurring in the high energy regions of the

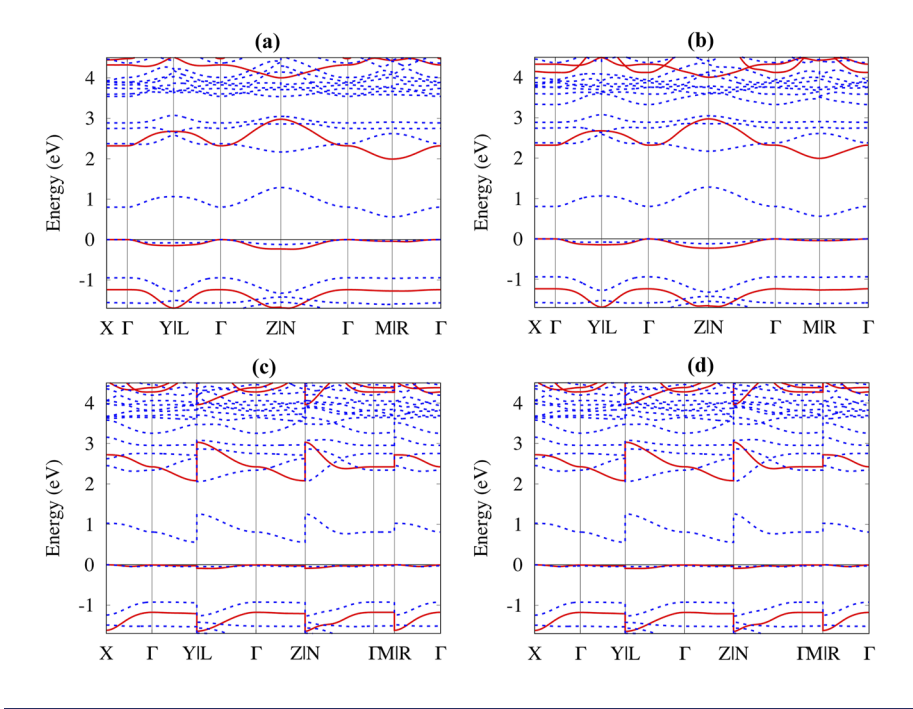


FIG. 3. Band structures of (a) TIPS-PEN L, (b) TIPS-PEN H, (c) TIPS-PEN BW L, and (d) TIPS-PEN BW H. L stands for the lower energy configuration, while H stands for the higher energy configuration, as defined in the upper panel of Fig. 2. Bands in solid red (dotted blue) are calculated at the G₀W₀ (DFT) level. The highest energies of valence band maximum are set to zero (eV). The definition of high symmetry k-points can be found in the work of Setyawan and Curtarolo.⁵¹

spectra. These results imply that side-chain disorder in these crystals has little effect on the electronic and optical properties. Therefore, we will only discuss results from the L configuration for the remainder of the paper.

Figure 2 shows the sulfur position and packing disorder considered for TES-ADT and diF-TES-ADT. In TES-ADT (diF-TES-ADT), the distances between the sulfur labeled 1 in red and that labeled 2 in blue are 8.80 (6.13), 6.43 (4.45), and 7.25 (4.58) Å in the AL, AH, and S configurations, respectively; the distances between sulfur 1 and sulfur 3 are 6.73 (8.54) Å in all three configurations. When comparing the total energies of these packing configurations, the further the sulfur atoms on neighboring molecules (intermolecular sulfur interactions) are from each other, e.g., the distances between the sulfur atoms labeled 1 and 2 in Fig. 2, the lower the total energy. This result implies that the sulfur atoms tend to avoid each other as much as possible to reach an enthalpic-driven low-energy structure.

The band structures of TES-ADT and diF-TES-ADT structures are shown in Fig. 5, and the relevant physical quantities are provided in Table II. Even though the band structures look similar in the AL, AH, and S configurations, the electronic band gaps differ considerably. The AL configuration has the largest electronic bandgap, while the AH configuration has the smallest; the difference between these gaps is about 0.1 eV at the DFT level and about 0.2 eV at the G_0W_0 level. The differences in G_0W_0 gaps propagate to the BSE absorption spectra shown in Fig. 6; some physical quantities from

 G_0W_0 -BSE calculations are listed in Table III. The AL configuration spectrum exhibits a blue shift compared to the spectra of the S and AH configurations. The first peaks in each spectrum result from the lowest singlet excitons; the eigenenergies (denoted by E_S in Table III) also correspond to the first peaks in Fig. 6. In both TES-ADT and diF-TES-ADT, the energy differences in the G_0W_0 electronic bandgaps and first singlet excitons between the AL and AH configurations are each about 0.2 eV, making the exciton binding energies (E_b^S) of the AL, AH, and S configurations nearly the same. The above results show that, unlike side-chain disorder, disorder in ADT backbones can significantly impact the electronic and optical properties.

The general procedures for molecular synthesis and the resulting sulfur positional disorder in the crystallographic information file (CIF) suggest that crystals of diF-TES-ADT and TES-ADT have ADT backbones with both anti- and syn-configurations. Such a situation suggests that the experimental absorption spectra for these materials may be combinations of the spectra from the AL, AH, and S configurations. To explore this, we implemented weighted averages of the AL, AH, and S configuration spectra—based on (i) the order of total energies (AL < S < AH), (ii) the sulfur occupancy percentages embedded in the CIF, and (iii) an additional assumption to maximize AH (though maintaining the constraint from the total energies)—to develop spectra to represent these mixed configurations in a single material. Based on this analysis, we analyzed a diF-TES-ADT packing structure composed of 84% AL, 4% AH, and

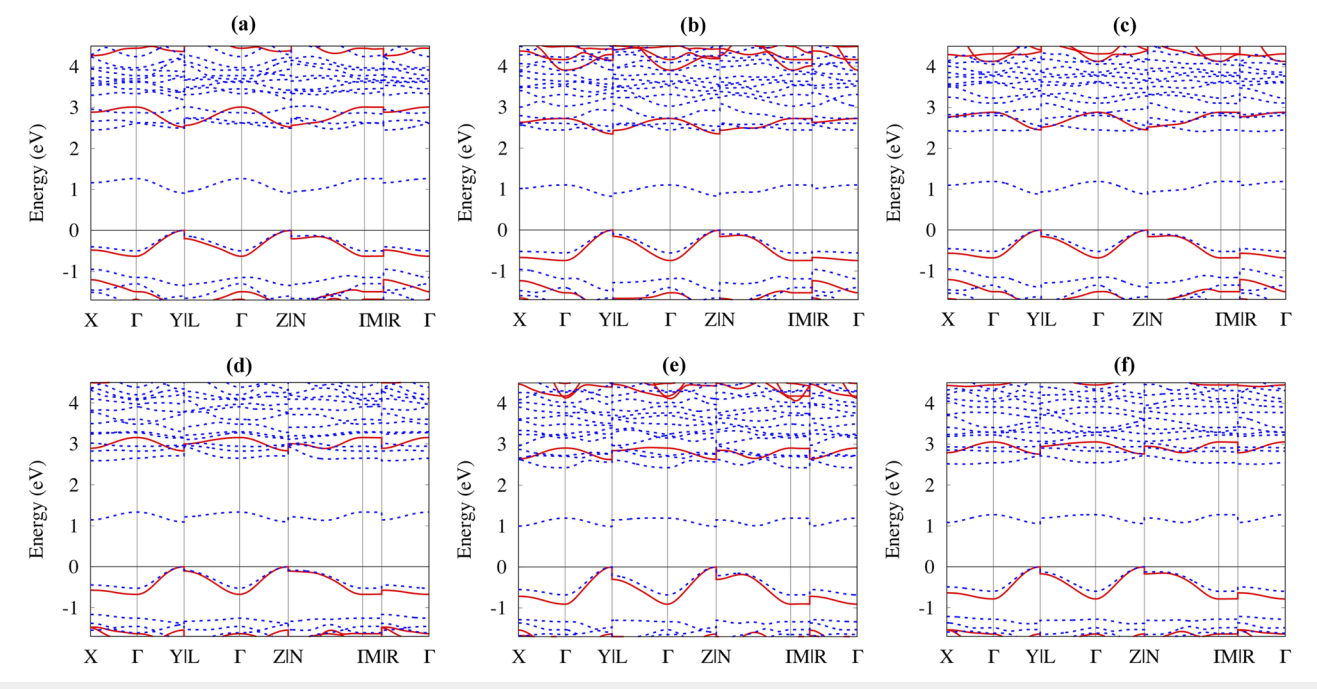


FIG. 5. Band structures of (a) TES-ADT AL, (b) TES-ADT AH, (c) TES-ADT S, (d) diF-TES-ADT AL, (e) diF-TES-ADT AH, and (f) diF-TES-ADT S. AL (AH) represents the anti-configuration with lowest (highest) total energy, while S represents the syn-configuration, as defined in the lower panel of Fig. 2. Bands in solid red (dotted blue) are calculated at the G₀W₀ (DFT) level. The valence band maxima are set to zero (eV). The definitions of high symmetry k-points can be found in the work of Setyawan and Curtarolo 51

TABLE II. Calculated electronic bandgap (E_g), bandwidths of the valence band (W_{VB}), and the conduction band (W_{CB}) at DFT and G_0W_0 levels for TES-ADT and diF-TES-ADT in different configurations. ΔE_g is the difference between G_0W_0 and DFT bandgaps. All energies are in eV.

Material and configuration	\mathbf{E}_{g}^{DFT}	\mathbf{E}_{g}^{GW}	ΔE_g	$W_{\mathit{VB}}^{\mathit{DFT}}$	$W_{\mathit{CB}}^{\mathit{DFT}}$	$\mathrm{W}_{\mathit{VB}}^{\mathit{GW}}$	$W_{\mathit{CB}}^{\mathit{GW}}$
TES-ADT AL	0.91	2.52	1.61	0.50	0.35	0.63	0.49
TES-ADT AH	0.82	2.35	1.53	0.56	0.28	0.74	0.38
TES-ADT S	0.88	2.45	1.57	0.53	0.31	0.68	0.43
diF-TES-ADT AL	1.09	2.83	1.74	0.52	0.24	0.67	0.33
diF-TES-ADT AH	0.99	2.63	1.64	0.68	0.21	0.91	0.29
diF-TES-ADT S	1.06	2.76	1.70	0.60	0.22	0.78	0.30

12% S and a TES-ADT packing structure composed of 54% AL, 14% AH, and 32% S. The weighted spectra are shown in Fig. 6. Since the AL configuration is dominant, the weighted spectra are each like the spectra of the respective AL configurations. Note that even with the large AH assumption, the AH configuration contributes little to the averaged spectra (shown on the lower energy side of the first strong peak); in other words, the first/lowest-energy exciton from the AL configuration is much brighter/stronger than that from the AH configuration even though the latter presents a lower-energy exciton. Based on this analysis, we propose that the small shoulder on the low-energy side of the first strong peak shown in the experimental absorption spectra [in Fig. 8(c)] for TES-ADT may arise from the presence of some AH configuration in an AL-dominant sample.

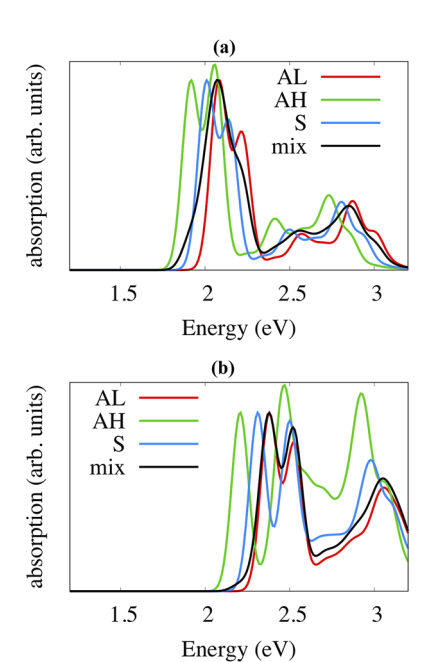


FIG. 6. Absorption spectra of (a) TES-ADT and (b) diF-TES-ADT by the G_0W_0 -BSE approach. The definitions of AL, AH, and S configurations can be found in the lower panel of Fig. 2. The black mixed curves (labeled by mix) are a mixture of AL, AH, and S configurations; more precisely, mix = 0.54 \times AL + 0.14 \times AH + 0.32 \times S for TES-ADT, whereas mix = 0.84 \times AL + 0.04 \times AH + 0.12 \times S for diF-TES-ADT. The intensities of the first peaks are normalized.

These results show that, strictly speaking, one should consider disorder in the ADT backbone for ADT derivatives when discussing their electronic and optical properties. However, a reasonable approximation is to only consider the lowest-energy, AL configuration in lieu of the weighted average. Here, of course, one would save tremendous computational cost and time. For this reason, OCELOT provides only calculated physical quantities from the AL configuration for ADT derivatives. For the remainder of this work, we only show the results from the AL configuration.

Electronic properties as a function of crystal packing

Figure 7 shows the DFT (blue dotted lines) and G_0W_0 (solid red lines) electronic band structures. The valence band maxima (VBM) are placed at the zero energy (in eV) in each plot; the definitions of high symmetry k-points in the Brillouin zones can be found in the work of Setyawan and Curtarolo. Select physical quantities extracted from the electronic band structures are listed in Table IV, including electronic bandgaps at both DFT (E_g^{DFT}) and G_0W_0 levels (E_g^{GW}), the difference between DFT and G_0W_0 gaps ($\Delta E_g = E_g^{GW} - E_g^{DFT}$), and VB and CB widths at both DFT and G_0W_0 levels. The G_0W_0 electronic bandgaps across the crystals range from 2.0 to 2.8 eV. All crystals present direct electronic gaps, with the exception of TIPG-PEN SS; for TIPG-PEN SS, the difference between the direct gap and the indirect gap is small (0.13 eV) due to its relatively flat VB and CB.

TABLE III. Fundamental/ G_0W_0 bandgap (E_g^{GW}), lowest singlet exciton energy (E_S), lowest triplet exciton energy (E_T), exciton binding energy with respect to the lowest singlet exciton (E_b^S), exciton binding energy with respect to the lowest triplet exciton (E_b^T), and energy conservation criterion for singlet fission ($E_S - 2E_T$) for TES-ADT and diF-TES-ADT in different configurations. All energies are in eV.

Material and configuration	\mathbf{E}_{g}^{GW}	E_S	\mathbf{E}_T	\mathbf{E}_b^S	E_b^T	$E_S - 2E_T$
TES-ADT AL	2.52	2.08	1.35	0.44	1.17	-0.62
TES-ADT AH	2.35	1.91	1.23	0.44	1.12	-0.55
TES-ADT S	2.45	2.01	1.29	0.44	1.16	-0.57
diF-TES-ADT AL	2.83	2.38	1.55	0.45	1.28	-0.72
diF-TES-ADT AH	2.63	2.21	1.48	0.42	1.15	-0.75
diF-TES-ADT S	2.76	2.31	1.52	0.45	1.24	-0.73

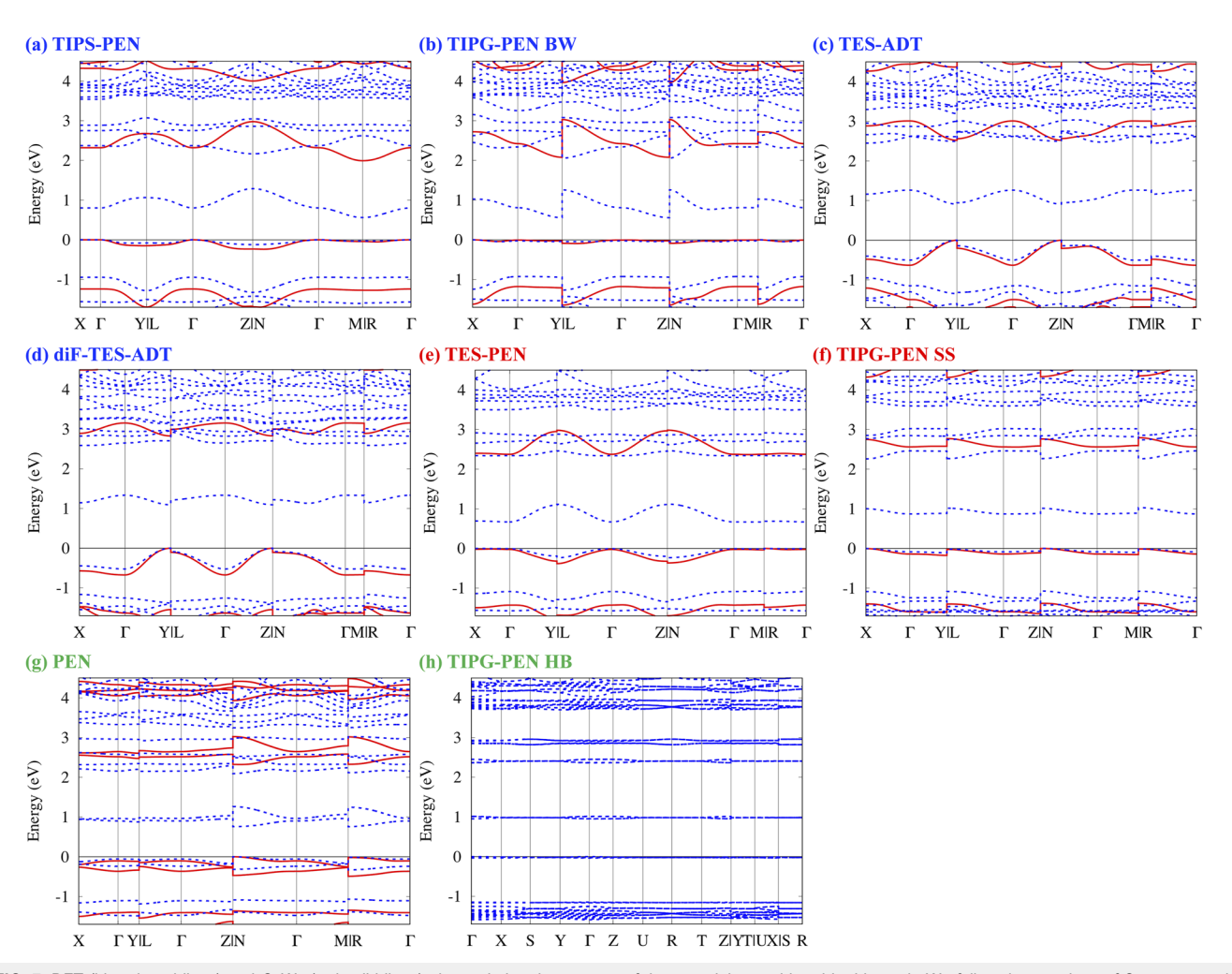


FIG. 7. DFT (blue dotted lines) and G_0W_0 (red solid lines) electronic band structures of the materials considered in this work. We follow the notations of Setyawan and Curtarolo to label high symmetry k-points in the Brillouin zone.⁵¹ The VB maxima are set to zero (eV) in each plot. (a)–(d) labeled in blue are categorized to the BW motif. (e) and (f) labeled in red belong to the SS motif. (g) and (h) labeled in green are classified in the HB packing motif.

TABLE IV. DFT (E_g^{DFT}) and G_0W_0 (E_g^{GW}) bandgaps of the materials considered in this work. $\Delta E_g = E_g^{GW} - E_g^{DFT}$. In each system, the former energy represents the indirect bandgap, while the latter energy represents the direct bandgap; however, for materials that are exactly direct-gap materials, only the direct bandgap is shown. Bandwidths of the VB (W_{VB}) and the CB (W_{CB}) at both DFT and G_0W_0 levels are also included. All energies are in eV. N.A. stands for not available.

Material	\mathbf{E}_{g}^{DFT}	E_g^{GW}	$\Delta \mathrm{E}_{g}$	$W_{\mathit{VB}}^{\mathit{DFT}}$	$W_{\mathit{CB}}^{\mathit{DFT}}$	$W_{\mathit{VB}}^{\mathit{GW}}$	$W_{\mathit{CB}}^{\mathit{GW}}$
TIPS-PEN	0.56/0.59	1.99/2.03	1.43/1.44	0.12	0.73	0.24	0.99
TIPG-PEN BW	0.56/0.60	2.08/2.10	1.52/1.50	0.05	0.70	0.09	0.95
TES-ADT	0.91	2.52	1.61	0.50	0.35	0.63	0.49
diF-TES-ADT	1.09	2.83	1.74	0.52	0.24	0.67	0.33
TES-PEN	0.67/0.68	2.37/2.38	1.70/1.70	0.23	0.45	0.38	0.62
TIPG-PEN SS	0.87/0.95	2.56/2.69	1.69/1.74	0.11	0.16	0.17	0.24
PEN	0.76	2.32	1.56	0.17	0.21	0.26	0.26
TIPG-PEN HB	0.95	N.A.	N.A.	0.02	0.03	N.A.	N.A.

VB and CB widths are proportional to the intermolecular electronic couplings among the molecules in the crystals and can provide insights into estimate aspects of the charge-carrier mobilities. Typically, a large bandwidth implies a large band curvature and a small effective carrier (hole, VB, or electron, CB) mass. As shown in Fig. 7, TIPG-PEN HB has a nearly flat VB and CB (the smallest W_{VB}^{DFT} and W_{CB}^{DFT} in Table IV). TIPG-PEN SS has slightly larger VB and CB widths. Although the VB width of TIPG-PEN BW is smaller than that of TIPG-PEN SS, the CB width is much larger than that in SS and HB packings. From Table IV, one can see that, in general, materials with the BW packing have moderately dispersive VB and/or CB, while materials with HB and SS packings (PEN, TIPG-PEN SS, and TIPG-PEN HB) are less dispersive. The calculated VB and CB widths are consistent with measured charge-carrier properties for the trialkyltetrelethynyl acenes, where materials with HB packing usually have smaller charge-carrier mobilities than materials with SS or, especially, BW packing. The exception is TES-PEN in the SS packing, where moderately dispersive VB and CB are comparable to those in diF-TES-ADT in the BW packing.

Optical properties as a function of crystal packing

Figure 8 shows calculated absorption spectra (solid red curves) via the G_0W_0 -BSE approach compared with the corresponding experimental data (dotted black and blue curves). Table V lists select physical quantities extracted from both the G_0W_0 -BSE calculations and available experimental data. The energies of the first peaks in the G_0W_0 -BSE absorption spectra are coincident with the energies of first/lowest-energy singlet excitons (denoted by E_S in Table V), i.e., the first allowed excitons are bright. We assume that the above statement is also true for the experimental data and, thus, denote the energy of the first peak in each experimental spectrum by $E_{S,exp}$. Comparing E_S and $E_{S,exp}$, one observes that the differences, $|\Delta E_S|$, are all \sim 0.1 eV, a typical difference noted for the G_0W_0 -BSE approach applied to OSCs. Furthermore, we note that, overall, the calculated absorption spectra are in good agreement with the experimental spectra, though the relative intensities of the peaks can differ.

Given that TIPG-PEN has known HB, SS, and BW crystal packings, we use these structures to focus on how the different packings

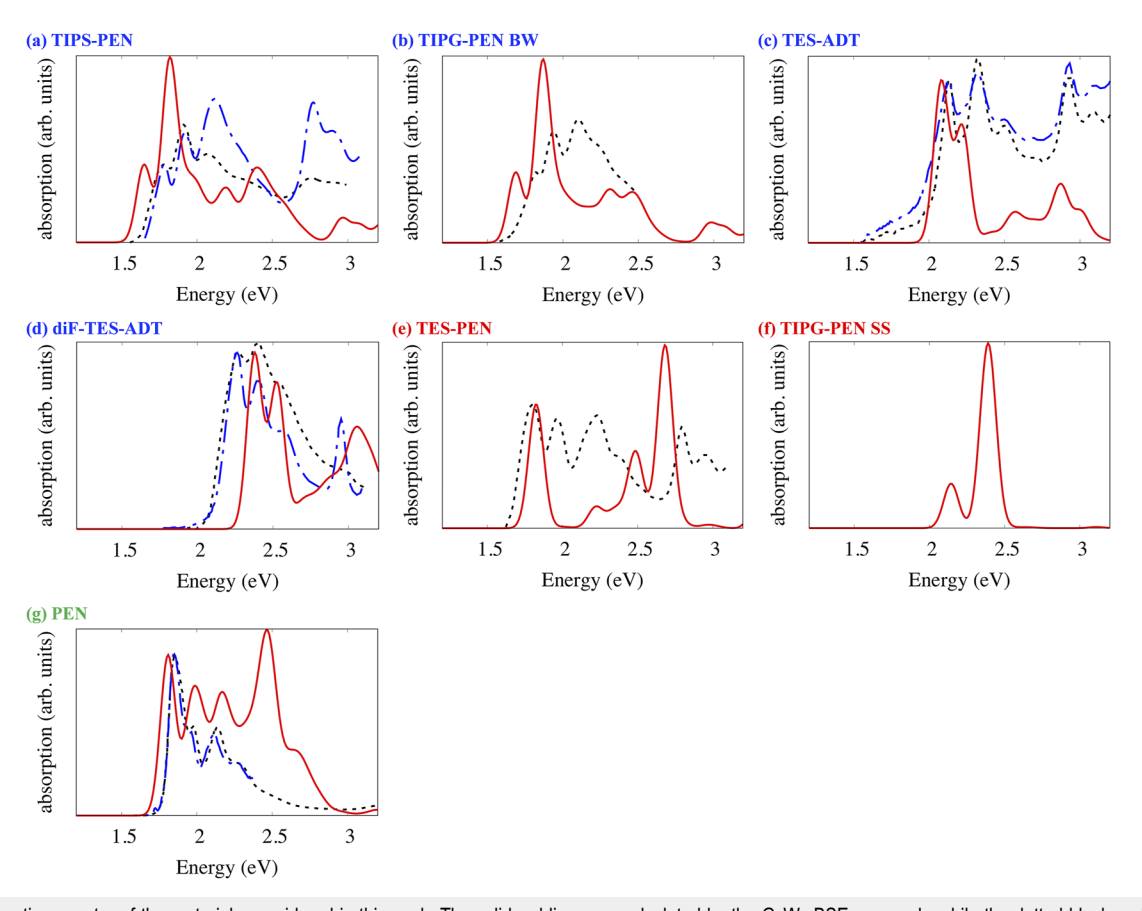


FIG. 8. Absorption spectra of the materials considered in this work. The solid red lines are calculated by the G_0W_0 -BSE approach, while the dotted black and blue lines are extracted from experimental spectra (if available, and the first peak intensities of calculated and experimental spectra are normalized). The black (blue) curve in (a) is extracted from Ref. 53 (Ref. 54). The experimental/black curve in (b) is extracted from Ref. 55. In (c), both experimental curves are extracted from Ref. 56. In (d), the black (blue) curve is extracted from Ref. 57 (Ref. 58). The experimental/black curve in (e) is extracted from Ref. 54. The black (blue) curve in (g) is extracted from Ref. 59 (Ref. 60). (a)–(d) labeled in blue are categorized to the BW motif. (e) and (f) labeled in red belong to the SS motif. (g) labeled in green is classified in the HB motif.

TABLE V. Direct G_0W_0 bandgap $(E_{g,d}^{GW})$, lowest singlet exciton energy (E_S) , lowest triplet exciton energy (E_T) , exciton binding energy with respect to E_S (E_b^S) , exciton binding energy with respect to E_T (E_b^T) , and energy conservation criterion for singlet fission $(E_S - 2E_T)$ of materials considered in this work. The energy of the first peak of an experimental absorption spectrum (shown in Fig. 8) is denoted by $E_{S,exp}$. $|\Delta E_S| = |E_{S,exp} - E_S|$. All energies are in eV. N.A. stands for not available.

Material	$\mathbf{E}_{g,d}^{GW}$	E_S	\mathbf{E}_T	E_b^S	\mathbf{E}_b^T	$E_S - 2E_T$	$E_{S,exp}$	$ \Delta E_{\mathcal{S}} $
TIPS-PEN	2.03	1.65	0.91	0.38	1.12	-0.17	1.78 ^a /1.78 ^b	0.13/0.13
TIPG-PEN BW	2.10	1.69	0.89	0.41	1.21	-0.09	1.82°	0.13
TES-ADT	2.52	2.08	1.35	0.44	1.17	-0.62	$2.14^{\rm d}/2.13^{\rm d}$	0.06/0.05
diF-TES-ADT	2.83	2.38	1.55	0.45	1.28	-0.72	$2.26^{\rm e}/2.26^{\rm f}$	0.12/0.12
TES-PEN	2.38	1.82	1.03	0.56	1.35	-0.24	1.80^{b}	0.02
TIPG-PEN SS	2.69	2.14	1.03	0.55	1.66	+0.08	N.A.	N.A.
PEN	2.32	1.81	1.02	0.51	1.30	-0.23	$1.85^{\rm g}/1.84^{\rm h}$	0.04/0.03

^aReference 53.

impact the optical properties. Figures 8(b) and 8(f) show that the first peak of TIPG-PEN in the SS packing shows a blue shift compared to that of the BW packing. The blue shift is significant (0.45 eV), making it a good fingerprint to distinguish BW and SS crystal structures. To further distinguish the origins of optical absorptions in TIPG-PEN BW and TIPG-PEN SS, we determined the imaginary parts of dielectric constants (denoted by ϵ_2) via different incident light polarizations (Fig. 9). From Figs. 9(b) and 9(f), we observe that the first peak in the BW packing arises from incident light polarized along the short axis, while the first peak in the SS packing results from light polarized along both the short and long axes. In addition, one observes that the second peak in the BW (SS) packing can only be observed when the incident light polarization is parallel to the long axis (short axis). These features reveal strong anisotropy in the optical properties of these materials and suggest parameters that can (further) be used to distinguish crystal structures of TIPG-PEN by polarized UV-vis absorption spectroscopy.

Figure 10 shows the exciton wavefunctions. From Figs. 10(b) and 10(f), for singlet excitons, one observes that TIPG-PEN SS exhibits an extremely strong charge-transfer (CT) character, as the electron and hole are localized on different molecules. On the other hand, the singlet exciton of TIPG-PEN BW shows an admixture of CT and Frenkel-like (localized) excitonic character. Hence, the optical properties of these molecular materials can change considerably if the crystal structures/packings differ, as previously shown for other OSCs 61

We now expand beyond TIPG-PEN to address whether one can distinguish the HB, SS, and BW packing of a molecular crystal if only the optical absorption spectra are known. To answer the question, we need to determine properties/features solely dependent on material packing. It may not be easy to achieve the goal if we solely rely on Fig. 8, in which, no matter whether we examine the calculated or experimental spectra, all spectra show several (two to six) peaks within the chosen energy range (1.2 – 3.2 eV) and the profiles are

generally similar. For example, the spectrum of TES-PEN does not look like the one of TIPS-PEN SS (both materials are in the SS packing). On the contrary, the experimental spectrum of TES-PEN is similar to the spectra of materials with the BW packing, including TIPS-PEN, TIPG-PEN BW, TES-ADT, and diF-TES-ADT. Therefore, it is difficult to say that materials with a particular packing will have similar absorption spectra. However, when we examine Fig. 9 (and Fig. 8), we find that the ϵ_2 spectra of TIPG-PEN SS and TES-PEN, except for the first peaks, mainly arise from the spectra with incident light that is polarized along the short axis of the pentacene backbone; on the contrary, ϵ_2 spectra of other materials arise from spectra with incident light polarized both along the short- and long-directions of the pentacene or ADT backbones. These differences relate to the fact that long-range π -stacking is 1D for the SS packing and 2D for the BW packing.

To verify our conjecture, we analyze the molecular configurations of TIPG-PEN SS (TES-PEN) in the crystal, where it is noted that the angle between the direction of 1D π -stacking and the shortaxis is 75° (82°), while the angle between 1D π -stacking and the long-axis is 28° (30°). The geometric analyses show that the short axis (long axis) is nearly perpendicular (parallel) to the direction of the 1D π stack.⁶² We further calculate ϵ_2 with incident polarized light exactly parallel (perpendicular) to the direction of 1D π stack, plotted in solid magenta (dotted green) in Figs. 9(h) and 9(i) for TES-PEN and TIPG-PEN SS, respectively. The geometric analyses and the similarities among spectra (e) and (h), and (f) and (i) as well, suggest that the direction of the long-range π stack is a special feature in materials with the SS packing. When incident light is polarized along the stacking direction of the π -conjugated backbones, the resulting absorption spectrum shows mainly the lowest singlet exciton; other excitons with higher energies can be observed with incident polarized light perpendicular to the direction of the π stack. In summary, the ϵ_2 spectrum of a material with the SS packing is dominated by incident light perpendicular to the

^bReference 54.

cReference 55.

^dReference 56.

eReference 57.

^fReference 58.

gReference 59.

^hReference 60.

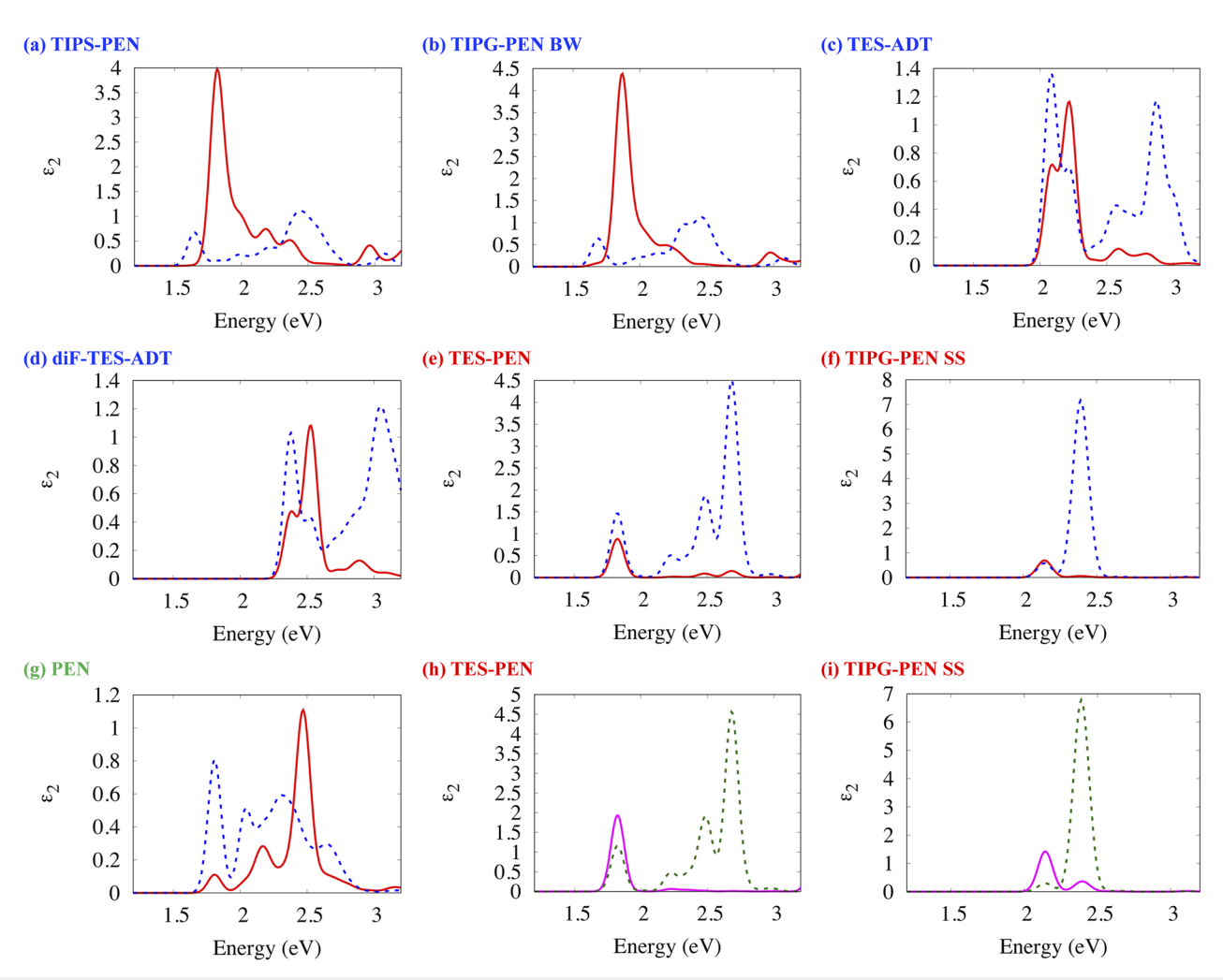


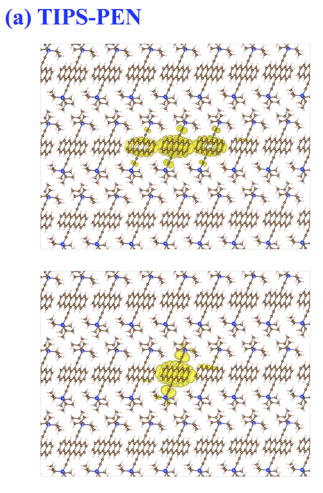
FIG. 9. Calculated ϵ_2 (the imaginary part of the dielectric constant) of the materials considered in this work. The solid red curves are obtained when incident light is polarized along the long-axis of the pentacene backbone, while the dotted blue curves are obtained when incident light is polarized along the short-axis of the pentacene backbone. In (h) and (i), the solid magenta (dotted green) curves are obtained when incident polarized light is parallel (perpendicular) to the direction of one dimensional π -stacking. (a)–(d) labeled in blue are categorized to the BW motif. (e), (f), (h), and (i) labeled in red belong to the SS motif. (g) labeled in green is classified in the HB motif.

 π stack. The ϵ_2 spectra of materials with HB and BW packings have contributions that more evenly arise from incident light polarized along both the short and long axis of the pentacene or ADT backbone.

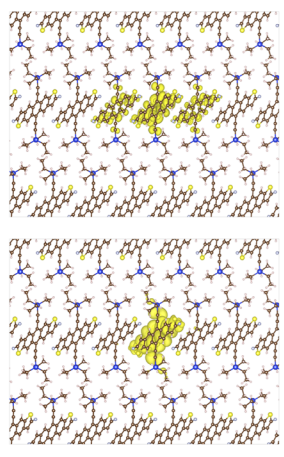
Evaluating the potential for singlet fission

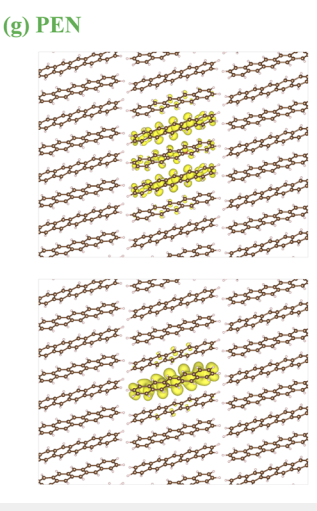
We now turn our attention to singlet fission. Organic solar cells are a promising alternative to inorganic solar cells because of the following: (i) They are comprised of earth-abundant elements; (ii) they can be flexible, semi-transparent, and lightweight; (iii) their electronic and optical properties can be tuned through straightforward chemical syntheses; and, (iv) they can be fabricated through solution processing methods that allow for large scale, and potentially lower cost, production. 61.63-69 The process of singlet (exciton) fission

makes organic materials even more attractive as it offers the potential for photovoltaic conversion efficiencies (PCEs) that go beyond the conventional Shockley–Queisser limit. $^{70-76}$ Singlet fission was first proposed in 1965 to explain the photophysics of anthracene crystals. 77 In short, singlet fission is a process by which a singlet exciton is converted to two triplet excitons. In a photovoltaic device, these triplet excitons can then be harvested by a companion material where each exciton can be converted to an electron and a hole—i.e., from a single photon, two electron–hole pairs can be formed. In 1961, Shockley and Queisser determined the upper PCE limits for p–n junction solar cells to be ~30%. In 2006, Hanna and Nozik showed that the maximum PCE for single gap photovoltaic devices with materials that undergo efficient singlet fission can approach 44%. From the viewpoint of energy conservation, the low-lying singlet (S1 state) exciton energy (denoted by Es) should be more

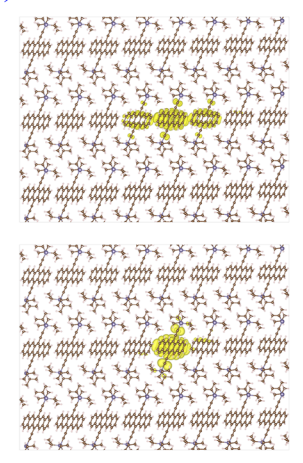




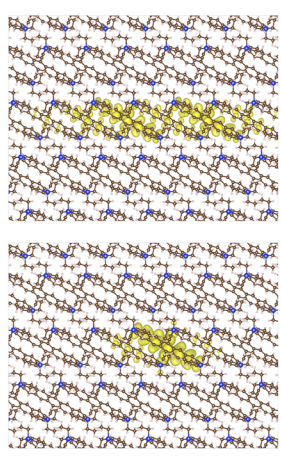




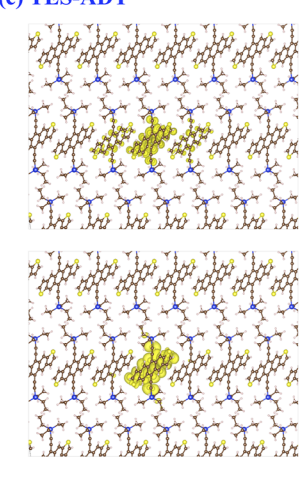
(b) TIPG-PEN BW



(e) TES-PEN



(c) TES-ADT



(f) TIPG-PEN SS

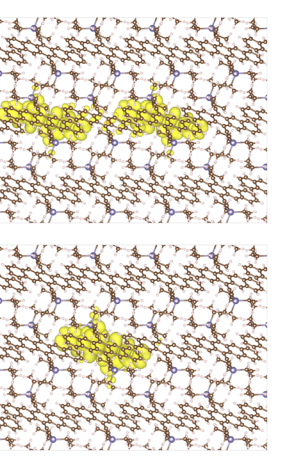


FIG. 10. Exciton wave functions of materials considered in this work. In each inset, the upper (lower) panel shows the first/lowest singlet (triplet) exciton wave function. (a)–(d) labeled in blue are categorized to the BW motif. (e) and (f) labeled in red belong to the SS motif. (g) labeled in green is classified in the HB motif.

than twice (2x) the triplet (T₁ state) exciton energy (denoted by E_T). This criterion is simple and intuitive, and is often used as a first determination as to whether a material is a good candidate singlet fission material or not.⁶⁷ Several OSCs exhibit singlet fission, including crystalline pentacene.75

We now turn to the G_0W_0 -BSE approach 52,53,61,81 to evaluate singlet fission energy conservation criteria for the pentacene and ADT-based materials considered here. To examine the potential for singlet fission, we need to understand the properties of the lowestenergy singlet and triplet excitons. We start by describing these exciton wave functions, 52,53,61,81 depicted in Fig. 10; in each inset, the upper panel shows the singlet exciton wave function, while the lower panel shows that for the triplet. In general, the triplet exciton wave functions are more localized than the singlets, as expected. Comparing the singlet exciton wave functions, we observe two categories: The first group, with TIPS-PEN, TIPG-PEN BW, TES-ADT, and diF-TES-ADT (each with the BW packing), shows large electron probability densities on the molecule where the hole resides, a more Frenkel-like (localized) exciton, while the adjacent (nearest) molecules have smaller electron probability densities. On the contrary, PEN, TIPG-PEN SS, and TES-PEN have electron probability densities on the hole-residing molecule that are smaller than those on the adjacent molecules. Among these materials, TIPG-PEN SS shows almost pure CT character, i.e., the electron and the hole are localized on different molecules; the other materials possess some CT and Frenkel-like character. From Table IV, we observe that materials in the first (second) group have dispersive (flatter) VB and CB, showing that a material with a more dispersive VB and CB leads to excitons with mixed CT and Frenkel character. The relatively flat bands in TIPG-PEN SS result in pure CT character.

The first triplet exciton energy in each material is given in Table V, denoted by E_T ; the exciton binding energy with respect to E_T , denoted by E_h^T , and those for the singlet states (E_h^S) are also provided. E_b^S show minimal deviation, ranging from 0.4 to 0.6 eV, though the G_0W_0 bandgaps ($E_{g,d}^{GW}$) and singlet exciton energies (E_S) fluctuate more, ranging from 2.0 to 2.8 and 1.7 to 2.4 eV, respectively. We note that the exciton binding energies (E_b^S) are sufficiently large; if they were too small, the singlet excitons may rapidly dissociate and, thus, decrease the singlet fission efficiencies. Since the singlet fission amounts to splitting a singlet exciton (with energy E_S) to two triplet excitons (each with energy E_T), one would expect that the energy conservation criterion, $E_S \approx 2E_T$, should be applicable. We, therefore, use $E_S - 2E_T$ as an energy conservation criterion for singlet fission; results for $E_S \approx 2E_T$ are provided in Table V (and Table III for higher energy configurations of TES-ADT and diF-TES-ADT). Experimentally, PEN, TIPS-PEN, and similar derivatives are well-known materials for efficient singlet fission.⁷ Interestingly, both TIPG-PEN in BW and SS packings exceed the energy conservation criterion for these studied materials, while TES-ADT and diF-TES-ADT do not; these results suggest that the ADT backbone is not favorable for singlet fission when compared to pentacene.

We considered two additional energy criteria of concern to singlet fission. To ensure that the two lowest triplet excitons (T₁ + T₁) will not annihilate to form the second-lowest triplet exciton (T_2) , i.e., $T_1 + T_1 \rightarrow T_2$, the energy of this second triplet exciton, denoted by $E(T_2)$, should ideally be larger than $2E_T$ (Table VI).

TABLE VI. Second energy criterion for singlet fission, $E(T_2) - E_S$, where $E(T_2)$ is the energy of the second triplet exciton (T_2) , E_T is the energy of the lowest triplet exciton, and E_S is the energy of the lowest singlet exciton.

Material	E(T ₂)	$E(T_2) - 2E_T$	$E(T_2) - E_S$
TIPS-PEN	1.73	-0.09	0.08
TIPG-PEN BW	1.74	-0.04	0.05
TES-ADT	2.15	-0.55	0.07
diF-TES-ADT	2.44	-0.66	0.06
TES-PEN	1.97	-0.09	0.15
TIPG-PEN SS	2.14	+0.08	0.00
PEN	1.86	-0.18	0.05

Here, with the exception of TIPG-PEN SS, $E(T_2)$ are each smaller than their respective $2E_T$ via the G_0W_0 -BSE approach, suggesting a potential competitive mechanism for singlet fission. Furthermore, to prevent intersystem crossing from S_1 to T_2 , $E(T_2)$ should be larger than the energy of the lowest singlet exciton (E_S), i.e., $E(T_2)$ > E_S. ^{92,93} Apart from TIPG-PEN SS, where E(T₂) is nearly identical to E_S , $E(T_2)$ are each slightly larger than the corresponding S_1 energies (ranging from 0.05 to 0.15 eV), suggesting that these materials may not suffer from this competitive mechanism for singlet fission.

CONCLUSIONS

Using the G₀W₀-BSE approach, we explored the electronic and optical properties of several OSC crystals of trialkyltetrelethynyl acenes. We first show how configurational disorder impacts electronic and optical properties: side-chain disorder has a limitedto-no effect on the material's electronic and optical properties, while heteroatom disorder in the ADT-based backbones can significantly affect the electronic bandgap (up to about 0.2 eV) and the first/lowest-energy singlet exciton. Although one should take a weighted average of physical quantities in materials with potential sub-configurations (i.e., the AL, AH, and S configurations of the ADT-based systems), the physical quantities determined from the lowest energy, highest-weight configurations (here, the AL configuration) are generally close in nature to the averaged

We next explore the electronic and optical properties of these materials by evaluating their G₀W₀ band structures, G₀W₀-BSE absorption spectra, polarized ϵ_2 spectra, and exciton wave functions; as one may expect, both the chemical molecular structures and solidstate packings influence each of these characteristics. The average VB and CB widths in a material with the SS packing can be comparable to that in a material with the BW or HB packing. The G_0W_0 -BSE absorption spectra agree well with experimental data (at least in terms of the first/lowest-energy peak positions, with errors of about 0.1 eV). The absorption spectrum of a material with the SS packing (e.g., TES-PEN) may be similar to that of a material with the BW packing (e.g., TES-ADT) but different from that of a material with the same SS packing (e.g., TIPG-PEN SS). Hence, it may be challenging to determine the packing of molecular crystals by solely examining their absorption spectra. To distinguish the SS packing from the BW and HB packings, however, polarized ϵ_2 spectra can

be used to achieve the goal due to the long-range, 1D π stacking in the SS packing. Apart from the first peak, the ϵ_2 spectrum with incident light perpendicular to the direction of π -stacking dominates in a material with the SS packing. On the contrary, the ϵ_2 spectra of materials with the BW and HB packings have contributions that arise from incident light polarized along both the short and long axis of the pentacene or ADT backbone. Analyses of the exciton wave functions reveal that flatter VB and CB tend to produce more CTlike singlet excitons. Finally, based on energy conservation criteria, we find that materials derived from molecules with the pentacene backbone should outperform those derived from molecules with the ADT backbone for singlet fission.

ACKNOWLEDGMENTS

This work was sponsored, in part, by the National Science Foundation through the Designing Materials to Revolutionize and Engineer our Future (NSF DMREF) program under Award No. DMR-1627428 and Cooperative Agreement No. 1849213. We acknowledge the University of Kentucky Center for Computational Sciences and Information Technology Services Research Computing for their fantastic support and collaboration and use of the Lipscomb Compute Cluster and associated research computing resources.

AUTHOR DECLARATIONS

Conflict of Interest

The authors have no conflicts to disclose.

Author Contributions

Ling-Yi Huang: Formal analysis (equal); Investigation (equal); Writing - original draft (equal); Writing - review & editing (equal). Qianxiang Ai: Formal analysis (equal); Investigation (equal); Writing - original draft (equal); Writing - review & editing (equal). Chad Risko: Conceptualization (lead); Project administration (lead); Supervision (lead); Writing - original draft (equal); Writing - review & editing (equal).

DATA AVAILABILITY

The data that support the findings of this study are available within the article or from the corresponding author upon reasonable request.

REFERENCES

- ¹J. Zhao et al., Nanoscale **10**, 5764 (2018).
- ²S. Tong, J. Sun, and J. Yang, ACS Appl. Mater. Interfaces **10**, 25902 (2018).
- ³ W. Tang et al., J. Mater. Chem. C 7, 790 (2019).
- ⁴U. Zschieschang and H. Klauk, J. Mater. Chem. C 7, 5522 (2019).
- ⁵H. Matsui, Y. Takeda, and S. Tokito, Org. Electron. 75, 105432 (2019).
- ⁶R. A. Nawrocki, Adv. Funct. Mater. **29**, 1906908 (2019).
- ⁷H. Zhu et al., Adv. Funct. Mater. **30**, 1904588 (2020).
- ⁸M. Ashizawa et al., Prog. Polym. Sci. **100**, 101181 (2020).
- ⁹Y. Wakayama et al., J. Mater. Chem. C 8, 10956 (2020).
- ¹⁰ J.-H. Jou et al., J. Mater. Chem. C 3, 2974 (2015).
- ¹¹R.-P. Xu, Y.-Q. Li, and J.-X. Tang, J. Mater. Chem. C 4, 9116 (2016).

- ¹²H.-W. Chen et al., Light: Sci. Appl. 7, 17168 (2018).
- ¹³ J.-H. Jou et al., J. Mater. Chem. C **6**, 11492 (2018).
- ¹⁴S. Shahnawaz et al., J. Mater. Chem. C 7, 7144 (2019).
- ¹⁵S. Sudheendran Swayamprabha et al., Adv. Sci. **8**, 2002254 (2021).
- ¹⁶G. Husevnova et al., Adv. Opt. Mater. 9, 2002040 (2021).
- ¹⁷S. Antohe *et al.*, Thin Solid Films **642**, 219 (2017).
- ¹⁸R. S. Gurney, D. G. Lidzey, and T. Wang, Rep. Prog. Phys. **82**, 036601 (2019).
- ¹⁹Y. Jin et al., Adv. Mater. **31**, 1900690 (2019).
- ²⁰J. Ajayan *et al.*, Superlattices Microstruct. **143**, 106549 (2020).
- ²¹ Y. Xu et al., Rep. Prog. Phys. 83, 082601 (2020).
- ²²Y. Cui, L. Hong, and J. Hou, ACS Appl. Mater. Interfaces 12, 38815 (2020).
- ²³ A. Wadsworth et al., Adv. Mater. **32**, 2001763 (2020).
- ²⁴O. Doat et al., Polym. Int. 71, 6 (2022).
- ²⁵C. Wang et al., Chem. Soc. Rev. 47, 422 (2018).
- ²⁶ X. Zhang, H. Dong, and W. Hu, Adv. Mater. **30**, 1801048 (2018).
- ²⁷ J. E. Anthony, Chem. Rev. **106**, 5028 (2006).
- ²⁸H. Dong et al., Adv. Mater. **25**, 6158 (2013).
- ²⁹T. L. Threlfall, Analyst **120**, 2435 (1995).
- ³⁰ M. Kuhnert-Brandstätter and M. Riedmann, Microchim. Acta **92**, 107 (1987).
- ³¹C. A. Hunter and J. K. M. Sanders, J. Am. Chem. Soc. 112, 5525 (1990).
- ³²C. R. Groom et al., Acta Crystallogr., Sect. B: Struct. Sci., Cryst. Eng. Mater. 72, 171 (2016).
- 33 Q. Ai et al., J. Chem. Phys. 154, 174705 (2021).
- 34 P. Giannozzi et al., J. Phys.: Condens. Matter 21, 395502 (2009).
- 35 P. Giannozzi et al., J. Phys.: Condens. Matter 29, 465901 (2017).
- ³⁶D. R. Hamann, Phys. Rev. B **88**, 085117 (2013).
- ³⁷J. P. Perdew, K. Burke, and M. Ernzerhof, Phys. Rev. Lett. 77, 3865 (1996).
- ³⁸ M. S. Hybertsen and S. G. Louie, *Phys. Rev. B* **34**, 5390 (1986).
- ³⁹ M. Rohlfing and S. G. Louie, Phys. Rev. B **62**, 4927 (2000).
- ⁴⁰J. Deslippe *et al.*, Comput. Phys. Commun. **183**, 1269 (2012).
- ⁴¹ T. Rangel et al., Phys. Rev. B **93**, 115206 (2016).
- ⁴²X. Leng et al., Phys. Chem. Chem. Phys. 18, 30777 (2016).
- ⁴³I. Tamm, J. Phys. USSR **9**, 449 (1945).
- ⁴⁴S. M. Dancoff, Phys. Rev. **78**, 382 (1950).
- 45 G. Pizzi et al., J. Phys.: Condens. Matter 32, 165902 (2020).
- ⁴⁶M. Mamada et al., ACS Appl. Mater. Interfaces 5, 9670 (2013).
- ⁴⁷D. Lehnherr et al., Org. Lett. 14, 3660 (2012).
- 48 M. Mamada et al., Org. Lett. 14, 4062 (2012).
- ⁴⁹R. K. Hallani *et al.*, Adv. Funct. Mater. **26**, 2341 (2016).
- 50 K. J. Thorley and C. Risko, J. Mater. Chem. C 4, 4040 (2016).
- ⁵¹ W. Setyawan and S. Curtarolo, Comput. Mater. Sci. 49, 299 (2010).
- ⁵²S. Sharifzadeh, J. Phys.: Condens. Matter **30**, 153002 (2018).
- ⁵³S. Sharifzadeh et al., Adv. Funct. Mater. **25**, 2038 (2015).
- 54 D. T. James et al., ACS Nano 7, 7983 (2013).
- ⁵⁵ J. C. Sorli *et al.*, Chem. Mater. **31**, 6615 (2019).
- ⁵⁶ J. Chen et al., Nanoscale **6**, 449–456 (2014).
- ⁵⁷ A. D. Platt et al., J. Phys. Chem. C **113**, 14006 (2009).
- ⁵⁸C. K. Yong et al., Nat. Commun. 8, 15953 (2017).
- ⁵⁹ A. Hinderhofer et al., J. Chem. Phys. 127, 194705 (2007). ⁶⁰S. Duhm et al., Appl. Phys. Lett. **94**, 033304 (2009).
- ⁶¹ X. Wang et al., CrystEngComm 18, 7353 (2016).
- ⁶²T. Nematiaram, D. Padula, and A. Troisi, Chem. Mater. **33**, 3368 (2021).
- 63 B. Kippelen and J.-L. Brédas, Energy Environ. Sci. 2, 251 (2009).
- 64T. M. Clarke and J. R. Durrant, Chem. Rev. 110, 6736 (2010).
- ⁶⁵ A. J. Heeger, Adv. Mater. **26**, 10 (2014).
- ⁶⁶K. A. Mazzio and C. K. Luscombe, Chem. Soc. Rev. 44, 78 (2015).
- ⁶⁷X. Liu, H. Chen, and S. Tan, Renewable Sustainable Energy Rev. **52**, 1527 (2015).
- 68 L. Ma et al., Chem. Commun. 56, 14337 (2020).
- ⁶⁹L. Hong et al., APL Mater. **8**, 120901 (2020).
- ⁷⁰ M. B. Smith and J. Michl, Chem. Rev. **110**, 6891 (2010).
- ⁷¹ M. B. Smith and J. Michl, Annu. Rev. Phys. Chem. **64**, 361 (2013).

- ⁷²J. Lee *et al.*, Acc. Chem. Res. **46**, 1300 (2013).
- ⁷³C. J. Bardeen, Nat. Mater. **13**, 1001 (2014).
- ⁷⁴C. J. Bardeen, Annu. Rev. Phys. Chem. **65**, 127 (2014).
- 75 M. Tabachnyk et al., Nat. Mater. 13, 1033 (2014).
- ⁷⁶N. J. Thompson et al., Nat. Mater. 13, 1039 (2014).
- 77 S. Singh et al., J. Chem. Phys. 42, 330 (1965).
- ⁷⁸W. Shockley and H. J. Queisser, J. Appl. Phys. **32**, 510 (1961).
- ⁷⁹ M. C. Hanna and A. J. Nozik, J. Appl. Phys. **100**, 074510 (2006).
- 80 A. Rao et al., J. Am. Chem. Soc. 132, 12698 (2010).
- ⁸¹ X. Liu et al., J. Phys.: Condens. Matter **32**, 184001 (2020).
- 82 C. Ramanan et al., J. Am. Chem. Soc. 134, 386 (2012).

- 83 B. J. Walker et al., Nat. Chem. 5, 1019 (2013).
- 84 J. Herz et al., J. Phys. Chem. A 119, 6602 (2015).
- ⁸⁵J. Zirzlmeier *et al.*, Proc. Natl. Acad. Sci. U. S. A. **112**, 5325 (2015).
- ⁸⁶L. Yang et al., Nano Lett. **15**, 354 (2015).
- 87 T. Sakuma et al., J. Phys. Chem. A 120, 1867 (2016).
- ⁸⁸J. K. G. Karlsson et al., J. Phys. Chem. Lett. **9**, 3934 (2018).
- 89 N. Alagna et al., J. Phys. Chem. B 123, 10780 (2019).
- ⁹⁰ N. V. Korovina, N. F. Pompetti, and J. C. Johnson, J. Chem. Phys. **152**, 040904 (2020).
- ⁹¹ F. A. Schaberle *et al.*, Chemistry **2**, 545 (2020).
- ⁹² A. Japahuge and T. Zeng, ChemPlusChem 83, 146 (2018).
- 93 O. El Bakouri *et al.*, J. Am. Chem. Soc. **142**, 5602 (2020).